

# Bayesian Inference of Nongravitational Perturbations from Satellite Observations

Lamberto Dell'Elce\*

*University of Liège, 4000 Liège, Belgium*

and

Ohad Ben-Yaacov<sup>†</sup> and Pini Gurfil<sup>‡</sup>

*Technion–Israel Institute of Technology, 32000 Haifa, Israel*

DOI: 10.2514/1.G000485

Gravitational and third-body perturbations can be modeled with sufficient precision for most applications in low Earth orbit. However, owing to severe uncertainty sources and modeling limitations, computational models of satellite aerodynamics and solar radiation pressure are bound to be biased. Aiming at orbital propagation consistent with observed satellite orbital dynamics, real-time estimation of these perturbations is desired. In this paper, a particle filter for the recursive inference and prediction of nongravitational forces is developed. Specifically, after assuming a parametric model for the desired perturbations, the joint probability distribution of the parameters is inferred by using a prescribed number of weighted particles, each consisting of one set of orbital elements and one set of parameters. The particle evolution is carried out by means of an underlying orbital propagator, and the Bayes rule is used to recursively update weights by comparing propagated orbital elements with satellite observations. The proposed formulation uses mean orbital elements as the only available measurements. This feature makes the algorithm a potentially valuable resource for space situational awareness applications, such as space debris trajectories prediction from two-line elements, or for onboard force estimation from Global Positioning System data. High-fidelity simulations show that nongravitational perturbations can be estimated with 20% accuracy.

## I. Introduction

**T**O DATE, satellite drag and solar radiation pressure (SRP) estimation were mostly carried out by means of high-sensitivity accelerometers [1]. Nonetheless, force estimators using only satellite observations were also proposed. The method of dynamic model compensation (DMC) was arguably the most popular example of this class [2]: first, an underlying parametric model of the unknown perturbation was adopted; then, the parameters of the model were assumed to be first-order Gauss–Markov processes and were appended to the state vector of a recursive estimator (most often an extended Kalman filter). Provided with sufficiently dense and accurate satellite observations (i.e., standard deviations of 5 m for the position and 1 mm/s for the velocity), DMC was successfully applied to the estimation of the atmospheric force [3]. However, no other process noise except the atmospheric force itself was considered in [3], so this result was arguably not representative of a real-life scenario. In addition, the requirements on the accuracy and rate of observations were extremely severe for several applications. In [4], forces on the order of  $10^{-3}$  N/kg were accurately estimated by means of DMC. Dense measurements and analogous noise to [3] were considered. Similar accuracy was obtained when differentiation of Global Positioning System (GPS) data was implemented [5]. However, this accuracy was far from being sufficient to estimate drag or SRP that, in general, was three or more orders of magnitude smaller. Real-time estimation of local atmospheric density variations was tackled in [6] by recursively computing corrections of the Jacchia 71 atmospheric model. Here, range data and information on the solar

and geomagnetic activity proxies were processed to carry out the estimation. Simultaneous estimation of both the ballistic coefficient and atmospheric density was then addressed in [7] by using real range data, where the separability and observability of the two quantities was demonstrated.

Batch estimators were used for ground-based estimation using observations [8]. In this case, measurement noise could be largely relaxed, e.g., two-line elements (TLEs) were used in [9], but they were not suitable for recursive implementation. An alternative approach based on optimal control policies was recently developed in [10]. This technique was able to account for both atmospheric drag and SRP and could be naturally extended to complex models of the force, but it was also unsuitable for recursive estimation.

In the broader context of Bayesian estimation of dynamical systems, sequential Monte Carlo (SMC) algorithms, which include particle filters, are valuable tools for optimally approximating the posterior distribution of hidden Markov processes [11,12]. Compared to Kalman filtering techniques, particle filters do not require any assumption on either the linearity of the system or the nature of the noise. Such generality is obtained at the price of a greater computational burden. Particle filters were used in several problems in astrodynamics, e.g., space object tracking [13], orbit determination [14,15], and relative state estimation [16,17]. However, to the best of our knowledge, there has not been an attempt of nongravitational force estimation using particle filters, which is available in the literature.

In this paper, we develop an SMC algorithm for the recursive inference of nongravitational perturbations from satellite observations with no supporting in situ acceleration measurements. Our approach is conceptually similar to DMC but, in addition to the aforementioned advantages and drawbacks of SMC, we show that the proposed algorithm provides good estimates of the nongravitational perturbations, even when fairly inaccurate measurements and a modest underlying propagator are used and no information on the current space weather is available. Under these conditions, the probability density function (PDF) of the prior and likelihood are highly non-Gaussian. In addition, severe uncertainty generally affects the prior knowledge of the parameters of the nongravitational model, i.e., drag and reflectivity coefficient. Hence, our method is capable of dealing with significant uncertainties and, through Bayesian inference, estimating the nonconservative forces. This is

Received 21 February 2016; revision received 8 August 2016; accepted for publication 9 August 2016; published online 24 October 2016. Copyright © 2016 by the American Institute of Aeronautics and Astronautics, Inc. All rights reserved. All requests for copying and permission to reprint should be submitted to CCC at [www.copyright.com](http://www.copyright.com); employ the ISSN 0731-5090 (print) or 1533-3884 (online) to initiate your request. See also AIAA Rights and Permissions [www.aiaa.org/randp](http://www.aiaa.org/randp).

\*Postdoctoral Researcher, Space Structures and Systems Laboratory, Aerospace and Mechanical Engineering Department; [lamberto.dellelce@ulg.ac.be](mailto:lamberto.dellelce@ulg.ac.be).

<sup>†</sup>Doctoral Student, Distributed Space Systems Laboratory, Faculty of Aerospace Engineering; [ohadby@technion.ac.il](mailto:ohadby@technion.ac.il).

<sup>‡</sup>Associate Professor, Distributed Space Systems Laboratory, Faculty of Aerospace Engineering; [pgurfil@technion.ac.il](mailto:pgurfil@technion.ac.il). Associate Fellow AIAA.

actually an alternative to current methods because it uses the full power of nonlinear estimation, whereas the extended Kalman filter cannot deal, by definition, with large uncertainties.

The filter developed herein works by updating the empirical distribution of a finite number of weighted particles. Each particle consists of one set of orbital elements and some parameters (e.g., drag and reflectivity coefficients) used to evaluate a prescribed parametric model for nongravitational forces. Particles are updated by means of an underlying orbital propagator, and they are assigned weights based on the error between propagated orbital elements and satellite observations. Secular effects of the nongravitational perturbations allow “good” particles to emerge when weights are recursively updated.

Mean orbital elements are exploited as the only measurements. They can be obtained either by converting GPS states using a contact transformation or by using TLEs. The first option is pursued in this paper. Such a transformation is undoubtedly a noise source, so that one may argue that direct GPS measurements should be used instead. Nonetheless, averaged elements have two compelling features: first, their dynamics exhibit robustness for mismodeling of high-degree gravitational harmonics; second, they pave the way to the exploitation of computationally efficient analytical and semi-analytical techniques (e.g., SGP4) to propagate particles.

The paper is organized as follows. Section II discusses the mathematical background on the SMC and outlines the algorithm of the filter. Section III details the different ingredients of the problem of nongravitational force estimation. Insight and caveats on the choice of the parameters of the filter are discussed as well. Finally, numerical simulations in a high-fidelity environment are carried out in Sec. IV.

## II. Sequential Monte Carlo for Parameter and State Estimation

Let  $\mathbf{P} \in \mathcal{I}_p$  and  $\{\mathbf{X}_\tau \in \mathcal{I}_X, \tau \in \mathbb{N}^+\}$  be an  $\mathcal{I}_p$ -valued vector of uncertain parameters and an  $\mathcal{I}_X$ -valued discrete-time  $(m+1)$ th-order Markov process indexed by nonnegative integers (namely,  $\tau \in \mathbb{N}^+$ ) and provided with transitional prior distribution:

$$\mathbf{X}_{\tau+1} | \mathbf{x}_\tau, \mathbf{x}_{\tau-1}, \dots, \mathbf{x}_{\tau-m}, \mathbf{p} \sim f(\mathbf{x}_{\tau+1} | \mathbf{x}_\tau, \dots, \mathbf{x}_{\tau-m}, \mathbf{p}) \quad \forall t \geq m \quad (1)$$

respectively; here,  $f(\mathbf{x}_{\tau+1} | \mathbf{x}_\tau, \dots, \mathbf{x}_{\tau-m}, \mathbf{p})$  is the PDF defining how the process evolves given outcomes of the parameters' vector and the past  $m+1$  realizations of the state, i.e.,  $\mathbf{P} = \mathbf{p}, \mathbf{X}_{\tau-j} = \mathbf{x}_{\tau-j} \forall j = 0, \dots, m$ . Some  $\mathcal{I}_Y$ -valued observations  $\{Y_\tau \in \mathcal{I}_Y, \tau \in \mathbb{N}^+\}$ , conditionally independent in time, are available:

$$Y_\tau | \mathbf{x}_\tau, \dots, \mathbf{x}_0, \mathbf{p} \sim g(y_\tau | \mathbf{x}_\tau, \mathbf{p}) \quad \forall t \geq 0 \quad (2)$$

The PDF  $g(y_\tau | \mathbf{x}_\tau, \mathbf{p})$  is referred to as marginal likelihood distribution. Equations (1) and (2) define a hidden Markov model (HMM).

The filtering problem consists of estimating the marginal posterior distribution of the process, which is the joint PDF of  $\mathbf{P}$  and  $\mathbf{X}_\tau$  conditional to the observations  $\mathbf{Y}_0, \dots, \mathbf{Y}_\tau$  [12]:

$$\text{pdf}(\mathbf{x}_\tau, \mathbf{p} | \mathbf{y}_0, \dots, \mathbf{y}_\tau) \propto g(\mathbf{y}_\tau | \mathbf{x}_\tau, \mathbf{p}) \text{pdf}(\mathbf{x}_\tau, \mathbf{p} | \mathbf{y}_0, \dots, \mathbf{y}_{\tau-1}) \quad (3)$$

The analogy with Kalman filtering is established by considering  $f$  and  $g$  as nonlinear and non-Gaussian generalizations of the predictor and innovation equations, respectively, and the marginal of the posterior distribution as the updated state and covariance estimates.

A closed-form solution of Eq. (3) is not generally available. Particle filters approximate the posterior by means of SMC sampling of Eq. (3). If direct sampling from  $\text{pdf}(\mathbf{x}_\tau, \mathbf{p} | \mathbf{y}_0, \dots, \mathbf{y}_{\tau-1})$  is not possible or inconvenient, an auxiliary proposal distribution of  $q(\mathbf{x}_{\tau+1}, \mathbf{p} | \mathbf{y}_{\tau+1}, \mathbf{x}_\tau, \dots, \mathbf{x}_{\tau-m})$  is used, yielding the importance sampling approach. In theory, any PDF can be used as importance distribution, provided that its support covers  $\mathcal{I}_X$  and  $\mathcal{I}_p$ . However, the adequate choice of the proposal distribution is crucial for

achieving good performance of the filter and avoiding degeneracy [18].

Several SMC formulations exist [11,12], but most of them do not consider parameter estimation. Our algorithm is mainly inspired by the work of Liu and West [19], which combined state and parameter estimation by means of artificial evolution and kernel smoothing of parameters. The filter works by propagating a set of  $n$  particles from  $\tau$  to  $\tau+1$ . Each particle consists of the last  $m+1$  states, a set of parameters, and a weight:

$$j\text{th particle} := \{\mathbf{x}_\tau^{(j)}, \dots, \mathbf{x}_{\tau-m}^{(j)}; \mathbf{p}_\tau^{(j)}; w_\tau^{(j)}\} \quad j = 1, \dots, n \quad (4)$$

Weights are nonnegative and satisfy  $\sum_{j=1}^n w_\tau^{(j)} = 1$

The notation  $\mathbf{p}_\tau^{(j)}$  indicates the outcome of  $\mathbf{P}$  for the  $j$ th particle at time  $\tau$ . A Monte Carlo approximation of the posterior at time  $t$  is given by the empirical measure

$$\text{pdf}(\mathbf{x}_\tau, \mathbf{p} | \mathbf{y}_0, \dots, \mathbf{y}_\tau) \approx \sum_{j=1}^n w_\tau^{(j)} \delta(\mathbf{x}_\tau - \mathbf{x}_\tau^{(j)}) \delta(\mathbf{p} - \mathbf{p}_\tau^{(j)}) \quad (5)$$

where  $\delta(\cdot)$  is the multidimensional Dirac delta function. We note that this measure is referred to as a PDF with an abuse of notation, since the Dirac delta function is not absolutely continuous with respect to the Lebesgue measure.

The procedure for the recursive update of the particles consists of three steps:

1) The first step is prediction. The prediction of the states is provided by their expected value at time  $\tau+1$ :

$$\tilde{\mathbf{x}}_{\tau+1}^{(j)} = \int_{\mathcal{I}_X} \mathbf{x}_{\tau+1} q(\mathbf{x}_{\tau+1}, \mathbf{p}_\tau^{(j)} | \mathbf{y}_{\tau+1}, \mathbf{x}_\tau^{(j)}, \dots, \mathbf{x}_{\tau-m}^{(j)}) d\mathbf{x}_{\tau+1}, \quad j = 1, \dots, n \quad (6)$$

Artificial evolution of the parameters using kernel smoothing consists of using a Gaussian mixture model (GMM) to update  $\mathbf{p}_\tau^{(j)}$  [19]. A prior update is given by the location of the GMM's kernels:

$$\tilde{\mathbf{p}}_{\tau+1}^{(j)} = \gamma \mathbf{p}_\tau^{(j)} + \frac{1-\gamma}{n} \sum_{i=1}^n \mathbf{p}_\tau^{(i)}, \quad j = 1, \dots, n \quad (7)$$

where  $\gamma \in [0, 1)$  is a discount factor for the dispersion of the variance of the parameters. Section III.B provides further insight into this parameter.

The weights of the mixture's kernels are computed with the outcomes of Eqs. (6) and (7):

$$\tilde{w}_{\tau+1}^{(j)} \propto w_\tau^{(j)} \alpha(\mathbf{y}_{\tau+1}, \tilde{\mathbf{x}}_{\tau+1}^{(j)}, \mathbf{x}_\tau^{(j)}, \dots, \mathbf{x}_{\tau-m}^{(j)}, \tilde{\mathbf{p}}_{\tau+1}^{(j)}) \quad (8)$$

Here, the function  $\alpha$  is defined as

$$\alpha(\mathbf{y}_{\tau+1}, \mathbf{x}_{\tau+1}, \mathbf{x}_\tau, \dots, \mathbf{x}_{\tau-m}, \mathbf{p}) = \frac{f(\mathbf{x}_{\tau+1} | \mathbf{x}_\tau, \dots, \mathbf{x}_{\tau-m}, \mathbf{p}) g(\mathbf{y}_{\tau+1} | \mathbf{x}_{\tau+1}, \mathbf{p})}{q(\mathbf{x}_{\tau+1}, \mathbf{p} | \mathbf{y}_{\tau+1}, \mathbf{x}_\tau, \dots, \mathbf{x}_{\tau-m})} \quad (9)$$

2) The second step is resampling. When multiple recursive updates are performed, weights might become unevenly distributed, with most of them approaching zero. When this happens, only one to very few particles efficiently contribute to the measure of Eq. (5), for which the variance degenerates and the posterior distribution is not adequately approximated, whereas the memory to store a particle and the computations involved in its update are independent of the specific value of the weight. In other words, a huge effort is devoted to propagating particles with vanishing weights, for which the contribution to Eq. (5) is negligible. This issue is referred to as degeneracy.

To prevent degeneracy from occurring, a new set of uniformly weighted particles is resampled from Eq. (5). This is achieved

by sampling  $n$  integer coefficients  $(k^{(j)})_{j=1, \dots, n}$  with values in  $\mathcal{I}_n = \{1, 2, \dots, n\}$  and corresponding probabilities  $\{\tilde{w}_{\tau+1}^{(1)}, \tilde{w}_{\tau+1}^{(2)}, \dots, \tilde{w}_{\tau+1}^{(n)}\}$ :

$$k^{(j)} \sim \text{mnpdf}\left(k | \mathcal{I}_n, w_{\tau+1}^{(1)}, \dots, w_{\tau+1}^{(n)}\right), \quad j = 1, \dots, n \quad (10)$$

Here,  $\text{mnpdf}(\cdot | \mathcal{I}_n, w_{\tau+1}^{(1)}, \dots, w_{\tau+1}^{(n)})$  denotes the  $\mathcal{I}_n$ -valued multinomial distribution. After resampling, predicted weights are reset to  $\tilde{w}_{\tau+1}^{(j)} = (1/n)$ ,  $j = 1, \dots, n$ .

Several existing algorithms perform resampling at each time step. Because secular effects of nongravitational forces need long observation windows to become appreciable, recursive updates are needed to identify good particles, i.e., good particles have to collect multiple “good marks” before they can be distinguished from bad ones. For this reason, we discourage systematic resampling in this problem. Hence, we resample only if both of the following conditions are satisfied: 1) At least  $r$  time steps elapse since the last resampling. 2) The degeneracy indicator  $1/\sum_{j=1}^n (\tilde{w}_{\tau+1}^{(j)})^2$  is below a prescribed threshold. We note that the indicator is in the range  $[1, n]$  and it equals the two corner cases 1 and  $n$  if either all weights but one are equal to zero or the particles are uniformly weighted, respectively.

If resampling does not occur, the weights  $\tilde{w}_{\tau+1}^{(j)}$  are not modified and  $k^{(j)} = j \forall j \in [1, n]$ .

3) The third step is update. As an update, all kernels of the GMM used for artificial evolution share the same variance:

$$\mathbf{V}_\tau = (1 - \gamma^2) \frac{1}{n-1} \sum_{j=1}^n (\mathbf{p}_\tau^{(j)} - \bar{\mathbf{p}}_\tau) (\mathbf{p}_\tau^{(j)} - \bar{\mathbf{p}}_\tau)^T \quad (11)$$

where  $\bar{\mathbf{p}}_\tau = (1/n) \sum_{i=1}^n \mathbf{p}_\tau^{(i)}$ . The coefficient  $(1 - \gamma^2)$  is introduced so that the unweighted mixture preserves both the mean and variance of the sample  $[\mathbf{p}_\tau^{(1)}, \mathbf{p}_\tau^{(2)}, \dots, \mathbf{p}_\tau^{(n)}]$ .

Hence, states and parameters are updated by sampling from the GMM and importance distribution, respectively:

$$\mathbf{p}_{\tau+1}^{(j)} \sim \mathcal{N}\left(\mathbf{p}_{\tau+1} | \tilde{\mathbf{p}}_{\tau+1}^{(k^{(j)})}, \mathbf{V}_\tau\right) \quad (12)$$

$$\mathbf{x}_{\tau+1}^{(j)} \sim q\left(\mathbf{x}_{\tau+1} | \mathbf{y}_{\tau+1}, \mathbf{x}_\tau^{(k^{(j)})}, \dots, \mathbf{x}_{\tau-m}^{(k^{(j)})}, \mathbf{p}_{\tau+1}^{(j)}\right) \quad (13)$$

$$w_{\tau+1}^{(j)} \propto \tilde{w}_{\tau+1}^{(j)} \frac{\alpha\left(\mathbf{y}_{\tau+1}, \mathbf{x}_{\tau+1}^{(j)}, \mathbf{x}_\tau^{(k^{(j)})}, \dots, \mathbf{x}_{\tau-m}^{(k^{(j)})}, \mathbf{p}_{\tau+1}^{(j)}\right)}{\alpha\left(\mathbf{y}_{\tau+1}, \tilde{\mathbf{x}}_{\tau+1}^{(k^{(j)})}, \mathbf{x}_\tau^{(k^{(j)})}, \dots, \mathbf{x}_{\tau-m}^{(k^{(j)})}, \tilde{\mathbf{p}}_{\tau+1}^{(k^{(j)})}\right)} \quad (14)$$

for  $j = 1, \dots, n$ .

### III. Nongravitational Force Estimation

After detailing the general algorithm in Sec. II, we now apply it to nongravitational force estimation: first, the various constituents of the filter are defined; second, the transitional, marginal likelihood and proposal PDF are inferred by means of maximum likelihood estimation; and, finally, an insight into the choice of the filter parameters is provided. All forces are taken to be per mass unit in what follows.

Let  $\Delta t$  and  $t_{\text{orb}}$  be the (dimensional) time step of the filter and the orbital period, respectively. Denote by  $\mathcal{E}_\tau \equiv \mathcal{E}(\tau \Delta t)$  the six-dimensional set of orbital elements at time  $\tau \Delta t$ . Its averaged counterpart  $\bar{\mathcal{E}}_\tau$  is defined as

$$\bar{\mathcal{E}}_\tau = \frac{1}{t_{\text{orb}}} \int_{-t_{\text{orb}}/2}^{t_{\text{orb}}/2} \mathcal{E}(\tau \Delta t + t) dt \quad (15)$$

Noisy observations of the averaged orbital elements are available. Although advanced models for the measurement noise can be exploited, additive noise  $\Xi_\tau$  is used in this work because it facilitates the inference of the PDF  $g$ . Thus, the measurement equation reads

$$\mathbf{Y}_\tau = \bar{\mathcal{E}}_\tau + \Xi_\tau \quad (16)$$

where  $\Xi_\tau | \bar{\mathcal{E}}_\tau \sim g_{\bar{\mathcal{E}}}(\xi_\tau | \bar{\mathcal{E}}_\tau)$  and  $g_{\bar{\mathcal{E}}}(\xi_\tau | \bar{\mathcal{E}}_\tau) \equiv g(\bar{\mathcal{E}}_\tau + \xi_\tau | \mathbf{x}_\tau)$ . Typical means to gather measurements of averaged elements include either converting osculating elements provided by GPS data with a contact transformation (e.g., by means of the Brouwer model [20]) or using TLEs, which are available for most low-Earth orbit objects. The former option is pursued in this paper, and a first-order Brouwer–Lyddane model is used [21]. Although the contact transformation is a noise source, exploiting averaged elements enhances the robustness for mismodeling of high-degree gravitational harmonics. In addition, analytical and semianalytical techniques can be naturally integrated into the algorithm to propagate particles.

Averaged elements constitute part of the state variables. In addition, the desired nongravitational force  $f^{(\text{ng})}$  is also included, so that

$$\mathbf{X}_\tau = \left\{ \begin{array}{c} \bar{\mathcal{E}}_\tau \\ f_\tau^{(\text{ng})} \end{array} \right\} \quad (17)$$

Let  $\dot{\mathcal{E}}(\mathcal{E}, f)$  be the right-hand terms of the Gauss variational equations (GVEs) for a prescribed set of osculating elements  $\mathcal{E}$  and a perturbing force  $f(\mathcal{E}, t)$ . In this work, we use equinoctial elements, for which the definition and corresponding GVEs are given in Appendix A. Averaging the GVEs and integrating from time  $\tau \Delta t$  to  $(\tau + 1) \Delta t$  yield the averaged increment from  $\bar{\mathcal{E}}_\tau$  to  $\bar{\mathcal{E}}_{\tau+1}$ :

$$\Delta \bar{\mathcal{E}}_\tau = \int_{\tau \Delta t}^{(\tau+1) \Delta t} \left( \frac{1}{t_{\text{orb}}} \int_{-t_{\text{orb}}/2}^{t_{\text{orb}}/2} \dot{\mathcal{E}}(\mathcal{E}(t+s), f(\mathcal{E}, t+s)) ds \right) dt \quad (18)$$

Because the GVEs are linear in the perturbing force, the propagation of averaged elements can be recast as

$$\bar{\mathcal{E}}_{\tau+1} = \bar{\mathcal{E}}_\tau + \Delta \bar{\mathcal{E}}_\tau^{(g)} + \Delta \bar{\mathcal{E}}_\tau^{(\text{ng})} + \Delta \bar{\mathcal{E}}_\tau^{(\text{noise})} \quad (19)$$

where  $\Delta \bar{\mathcal{E}}_\tau^{(g)}$  and  $\Delta \bar{\mathcal{E}}_\tau^{(\text{ng})}$  denote the contributions to  $\Delta \bar{\mathcal{E}}_\tau$  due to gravitational and nongravitational perturbations, respectively;  $\Delta \bar{\mathcal{E}}_\tau^{(\text{noise})}$  includes the effects of all remaining nonmodeled forces, e.g., truncated gravitational harmonics, tides, and relativistic effects. The aforementioned underlying propagator defines which perturbations are included in  $\Delta \bar{\mathcal{E}}_\tau^{(g)}$ , and it approximates  $(\Delta \bar{\mathcal{E}}_\tau^{(g)} + \Delta \bar{\mathcal{E}}_\tau^{(\text{ng})})$ . For the sake of conciseness, integration errors are not explicitly mentioned in Eq. (19), but they are automatically accounted for while estimating the HMM according to Sec. III.A. The remaining perturbation  $\Delta \bar{\mathcal{E}}_\tau^{(\text{noise})}$  is modeled as an  $\mathcal{I}_{\bar{\mathcal{E}}}$ -valued stochastic process distributed according to

$$\Delta \bar{\mathcal{E}}_\tau^{(\text{noise})} \Big| \left( \bar{\mathcal{E}}_\tau, \dots, \bar{\mathcal{E}}_{\tau-m} \right) \sim f_{\bar{\mathcal{E}}}(\xi_\tau | \bar{\mathcal{E}}_\tau, \dots, \bar{\mathcal{E}}_{\tau-m}) \quad (20)$$

Parametric models of the aerodynamic and SRP perturbations are used to propagate  $f_\tau^{(\text{ng})}$ :

$$f_{\tau+1}^{(\text{ng})} = \Lambda_\tau^T \left\{ \begin{array}{c} f^{(\text{drag})}(\bar{\mathcal{E}}_\tau + \Delta \bar{\mathcal{E}}_\tau, \mathbf{p}_\tau, (\tau + 1) \Delta t) \\ f^{(\text{srp})}(\bar{\mathcal{E}}_\tau + \Delta \bar{\mathcal{E}}_\tau, \mathbf{p}_\tau, (\tau + 1) \Delta t) \end{array} \right\} \quad (21)$$

$$\Lambda_\tau \Big| \left( f_\tau^{(\text{ng})}, \dots, f_{\tau-m}^{(\text{ng})}, \mathbf{p} \right) \sim f_\Lambda(\lambda_\tau | f_\tau^{(\text{ng})}, \dots, f_{\tau-m}^{(\text{ng})}, \mathbf{p}) \quad (22)$$

Here,  $\{\Lambda_\tau \in (\mathbb{R}^+)^2, \tau \in \mathbb{N}^+\}$  is an  $(\mathbb{R}^+)^2$ -valued multiplicative noise modeling aleatory uncertainties, e.g., due to solar and geomagnetic activity or attitude of a tumbling debris. In this work,  $f^{(\text{drag})}$  and  $f^{(\text{srp})}$  read

$$f^{(\text{drag})}(\bar{\mathcal{E}}, \mathbf{p}, t) = -\frac{1}{2} \rho(\bar{\mathcal{E}}, \mathbf{p}) C_b(\mathbf{p}, t) v_{\text{tas}} v_{\text{tas}} \quad (23)$$

$$f^{(\text{stp})}(\bar{\mathcal{E}}, \mathbf{p}, t) = \begin{cases} 0 & \text{if } \mathbf{r} \cdot \frac{\mathbf{r}_\odot}{r_\odot} > 0 \text{ and } \left\| \mathbf{r} - \left( \mathbf{r} \cdot \frac{\mathbf{r}_\odot}{r_\odot} \right) \frac{\mathbf{r}_\odot}{r_\odot} \right\| \leq r_{\text{eq}} \\ -P_\odot C_r(\mathbf{p}) \frac{S_{\text{stp}}(t) r_\odot}{m r_\odot} & \text{otherwise} \end{cases} \quad (24)$$

where  $v_{\text{tas}}(\bar{\mathcal{E}})$ ,  $\mathbf{r}(\bar{\mathcal{E}})$ ,  $m$ ,  $S_{\text{stp}}$ ,  $P_\odot(t) = 4.56 \cdot 10^{-6} \text{ N/m}^2$ ,  $r_\odot(t)$ , and  $r_{\text{eq}}$  are the satellite's velocity with respect to the atmosphere, its position, mass, and cross-sectional area with respect to the sun direction, the radiation pressure, the sun position vector in astronomical units, and the mean equatorial radius, respectively; the atmospheric density  $\rho$ , ballistic coefficient  $C_b$ , and reflectivity coefficient  $C_r$  are prescribed parametric models, e.g., exponential atmosphere or harmonic expansion as illustrated in the case study detailed in Sec. IV.D; temporal variations of  $C_b$  and  $S_{\text{stp}}$  are due to available information on attitude dynamics. Indeed, more advanced models can be used but the specific underlying propagator may limit their choice. This is further discussed in Sec. IV, where the performance of two propagators is compared.

Finally, the process noise due to  $\Delta \mathcal{E}_\tau$  and  $\Lambda_\tau$  can reasonably be assumed as statistically independent, yielding

$$f(\mathbf{x}_{\tau+1}(\xi_\tau, \lambda_\tau) | \mathbf{x}_\tau, \dots, \mathbf{x}_{\tau-m}, \mathbf{p}) \equiv f_{\bar{\mathcal{E}}}(\xi_\tau | \bar{\mathcal{E}}_\tau, \dots, \bar{\mathcal{E}}_{\tau-m}) f_\Lambda(\lambda_\tau | f_\tau^{(\text{ng})}, \dots, f_{\tau-m}^{(\text{ng})}, \mathbf{p}) \quad (25)$$

where  $\mathbf{x}_{\tau+1}(\xi_\tau, \lambda_\tau)$  denotes the outcome of  $\mathbf{X}_{\tau+1}$  given the realizations  $\xi_\tau$  and  $\lambda_\tau$  of the processes defined in Eqs. (20) and (22), respectively.

#### A. Inference of the Hidden Markov Model via Maximum Likelihood Estimation

Targeting practical implementation of the filter, a model of the importance distribution  $q$  and of the various PDFs of the HMM (namely,  $g_{\bar{\mathcal{E}}}$ ,  $f_{\bar{\mathcal{E}}}$ , and  $f_\Lambda$ ) is required. This can be achieved by means of maximum likelihood estimation, which involves selecting an adequate "labeled" PDF (e.g., multivariate Gaussian or mixture model) followed by inferring suitable values to its parameters from available data.

Consider a set of  $n$  samples  $s_1, \dots, s_n$  of a random variable  $S$  and a PDF  $p_S(s; \boldsymbol{\theta})$ , where  $\boldsymbol{\theta}$  is the set of parameters defining the distribution, e.g., the mean and variance for a Gaussian distribution. According to the maximum likelihood method, these parameters are chosen such that they are consistent (e.g., positive definite covariance) and maximize the log-likelihood function

$$\mathcal{L}(\boldsymbol{\theta}) = \sum_{j=1}^n \log(p_S(s_j | \boldsymbol{\theta})) \quad (26)$$

In this work, we use GMMs as labeled distributions. Hence,  $\boldsymbol{\theta}$  consist of the weights, means, and variances of the kernels. GMMs provide flexibility in the representation of both marginal distributions and correlations. In addition, samples can be easily drawn from GMMs and their evaluation is straightforward.

The uncertainty characterization proposed in [22] is used to generate samples of the "true" averaged elements. For this purpose, the outer and inner integrals of Eq. (18) are accurately evaluated by means of the Dormand–Prince method based on a seventh-order Runge–Kutta method followed by high-order Gauss quadrature, respectively.

#### B. Considerations for the Choice of the Filter Parameters

A satisfactory tradeoff between accurate and rapid convergence is achieved by carefully setting up the parameters of the filter. The first parameter to consider is the number of particles  $n$ . Increasing  $n$  nearly linearly increases the overall computational burden. However, there must be enough particles to adequately represent the posterior

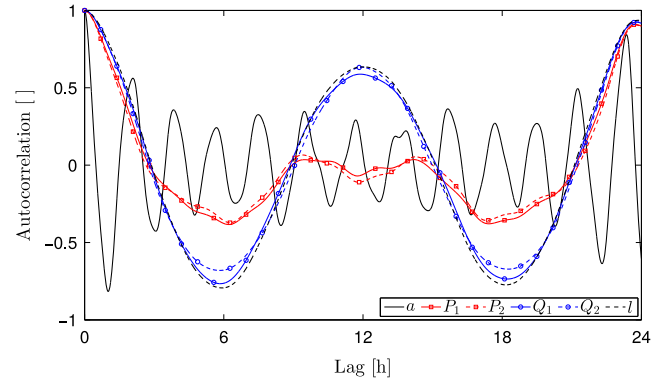


**Fig. 1** Autocorrelation of the process noise of averaged elements using the analytical propagator.

distribution and to delay degeneracy. This is particularly true during the early phase of the estimation, when uncertainty in the parameters  $\mathbf{p}$  is still very large. An adaptive choice of  $n$  is encouraged. This can be achieved during the resampling step.

Because of the aforementioned secular effects of nongravitational perturbations, and because measurement are statistically independent of time, increasing the filter's time step  $\Delta t$  and resampling rate  $r$  enhances the signal-to-noise ratio and, as such, improves the convergence of the estimation. Augmenting  $r$  is preferred when high-fidelity models of the nongravitational force are used because large time steps will reduce sensitivity to short-period variations. Nonetheless, degeneracy may occur for large  $r$ . Based on our experience, the product  $r\Delta t$  should be on the order of one-to-few orbital periods.

Neglected gravitational harmonics are the major source of process noise for averaged orbital elements. The order of the HMM ( $m+1$ ) is a crucial parameter for mitigating their impact. Specifically, Earth's rotation causes relevant correlations in the time series of the noise after about one day. For example, Fig. 1 depicts the autocorrelation of the process noise of the averaged orbital elements for the case study detailed in Sec. IV. Ideally, the order of the HMM should be large enough to cover this interval, but this may dramatically increase the required memory to store particles and augment the complexity of the importance and marginal prior distribution. Figure 1 also shows that all autocorrelations are close to one when the time step is below 10 min; so, we suggest using  $m=1$  if the filter's time step is of this order of magnitude. In this case, using  $m=0$  would result in extremely severe process noise, whereas larger  $m$  would be an unnecessary waste of computational resources.

Finally, the parameter  $\gamma$  regulates the memory of the particles: according to Eqs. (7) and (11), the parameters  $\mathbf{p}$  are nearly unchanged after being updated if  $\gamma \simeq 1$ ; on the contrary, they lose most memory of their previous value if  $\gamma \simeq 0$ . According to [19], values between 0.96 and 0.99 are reasonable for this parameter. We sustain this recommendation herein, owing to the need for multiple updates to identify good particles.

Table 1 summarizes all these caveats.

## IV. Numerical Simulations

The simulations discussed herein have a twofold objective, namely, providing some easily reproducible results and illustrating how the filter behaves in a realistic environment. For this purpose, four scenarios of increasing complexity are addressed. They differ in both the simulated environment and the underlying filter's propagator.

The simulated environment can be one of the following:

1) The first environment is low precision. Only Earth's oblateness and the drag force are modeled. The atmospheric density is assumed to be uniform, and the ballistic coefficient is given by

**Table 1** Influence of the filter's parameters on the quality of the estimation

Parameter	Benefits when increased	Drawbacks when increased
$n$	Enhanced representation of the posterior Convergence when $\mathbf{p}$ has large variance	Computational cost increases
$\Delta t$	Improved signal-to-noise ratio	Low sensitivity to short-period variations
$r$	Improved signal-to-noise ratio	Degeneracy might occur
$m$	Reduced sensitivity to process noise Enhanced convergence	Increased memory to store particles Increased complexity PDFs
$\gamma$	Enhanced identification of good particles	Diversity particles after multiple updates

$$C_b(t) = \frac{C_d}{m} (S_d(t) + S_{d,0}) \quad (27)$$

where  $C_d$  and  $S_{d,0}$  are the drag coefficient and a constant cross-sectional area, respectively.

2) The second environment is high-precision orbit propagation (HPOP) with constant solar activity. Gravitational harmonics up to the order and degree of 10, third-body perturbations of the sun and moon, aerodynamic force, and SRP are accounted for. The Sentman model is used to compute the aerodynamic force as a function of the geometric and ballistic properties of the satellite, as described in [23]. Variable accommodation of the energy and thermal flow are assumed, and the NRLMSISE-00 [24] atmospheric model is used. A parallelepiped-shaped satellite is considered, and the attitude is such that one geometrical axis points toward the orbital angular momentum vector; whereas the pitch angle, which is defined as the angle between the orbital velocity and the normal to the smallest face of the parallelepiped, is imposed.

3) The third environment is HPOP with time-varying solar activity. The same perturbations of the previous environment are accounted for. The historical data of the solar activity are used.

Two different propagators are implemented in the filter:

1) The first propagator is analytical. This is based on the analytical model proposed in [25] and outlined in Appendix B, which assumes an oblate planet and uniform atmosphere, i.e., vertical rarefaction, day–night bulge, and all other temporal and spatial variations of the atmospheric density are neglected. The low computational cost comes to the price of restrictions on the nongravitational force model, which needs to be consistent with the aforementioned assumptions. Specifically, SRP is neglected, and only the averaged drag can be estimated. The vector of parameters is  $\mathbf{p} = [C_d, S_{d,0}]^T$ .

2) The second propagator is numerical. This propagator lies on the other side of the spectrum and consists of brute force integration of Eq. (6), which enables extreme flexibility. Hence, the 20th-order Gauss quadrature and trapezoidal rule are used to compute the inner and outer integrals, respectively. The term  $\Delta\mathcal{E}_r^{(g)}$  includes gravitational harmonics up to the order and degree of four and third-body perturbations of the sun and moon. Both SRP and instantaneous atmospheric force are estimated. For this purpose, the atmospheric density is expanded in Fourier series to account for near-periodic variations due to orbital eccentricity, atmospheric bulge, and Earth's oblateness:

$$\rho = \rho_0 \left[ 1 + \sum_{j=1}^{n_{\text{exp}}} (c_j \cos(jL) + s_j \sin(jL)) \right] \quad (28)$$

where  $c_j$ ,  $s_j$ ,  $n_{\text{exp}}$ , and  $L$  denote the coefficients, the order of the expansion, and the true longitude defined in Appendix A, respectively. The vector of parameters is thus

$$\mathbf{p} = [C_d, S_{d,0}, c_1, s_1, \dots, c_{n_{\text{exp}}}, s_{n_{\text{exp}}}, C_r]^T$$

Appending  $\rho_0$  to  $\mathbf{p}$  is useless because  $\rho_0$  is systematically multiplied by  $C_d$ . Choosing an arbitrary  $\rho_0$  in the filter may shift the values of  $C_d$ , but it does not affect the error in the atmospheric force. For long-term scenarios, an exponential term has to be introduced in Eq. (28) to account for the vertical rarefaction due to orbital decay.

**Table 2** Simulated environment and underlying propagator for the various case studies

	Filter's propagator	Environment
Scenario 1	Analytical	Low-fidelity ( $J_2$ + uniform atmosphere)
Scenario 2	Analytical	HPOP, constant solar activity
Scenario 3	Analytical	HPOP, time-varying solar activity
Scenario 4	Numerical	HPOP, time-varying solar activity

**Table 3** Parameters of the simulations

	Value	Scenario
Initial orbital elements		
Semimajor axis	6828.137 km	1–4
Eccentricity	$10^{-3}$	1–4
Inclination	98 deg	1–4
Argument of perigee	120 deg	1–4
Right ascension of the ascending node	30 deg	1–4
True anomaly	15 deg	1–4
Epoch	4 Jan. 2012	2–4
Ballistic properties		
Mass	3 kg	1–4
Size	$0.3 \times 0.1 \times 0.1$ m	1–4
Pitch	$0.35\pi(t/t_{\text{orb}})$	1–4
Drag coefficient	2.2	1
	Modeled	2–4
Surface $S_{d,0}$	$5 \cdot 10^{-3}$ m <sup>2</sup>	1
	Modeled	2–4
Atmospheric modeling		
Density	$2.4 \text{ g} \cdot \text{km}^{-3}$	1
Daily and 81-day averaged solar activity $F_{10.7}$	150	2
	Historical data	3–4
Geomagnetic index $K_p$	4	2–4
Filter parameters		
Number of particles $n$	$\in [100, 3000]$	1–4
Filter's time step $\Delta t$	$t_{\text{orb}}$	1
	60 min	2–3
	3 min	4
Resampling rate $r$	$\text{ceil}(t_{\text{orb}}/\Delta t)$	1–4
HMM order $m$	0	1
	2	2
	3	3
	1	4
Discount factor $\gamma$	0.99	1–4
Number of kernels of the GMM	1	1
	5	2–4
Order of the Fourier expansion $n_{\text{exp}}$	2	4

The specific environment and propagator used in the four scenarios and the simulation setup are detailed in Tables 2 and 3, respectively. Scenarios 1 to 3 estimate a total of eight variables (i.e., six states and two parameters), whereas scenario 4 estimates 13 variables (i.e., six states and seven parameters). The number of samples is adapted during the resampling step. Specifically,  $n$  is reduced by 1% whenever at least 100 distinct coefficients  $k^{(j)}$  are extracted from the multinomial distribution. On the contrary,  $n$  is increased by 5% when this condition is not satisfied. We note that adapting the number of particles is not of use for a real-life onboard implementation. However, this is done here because we want to show

that the filter is able to converge even with a very broad and inaccurate PDF of  $p$ . However, this requires a rather large number of samples in the early phases of the estimation to adequately cover  $\mathcal{I}_p$ .

Measurement noise is mainly due to the first-order Brouwer–Lyddane contact transformation [21]. In addition, GPS noise is modeled as noncorrelated white noise with a standard deviation equal to 5 m and 2 cm/s for the position and velocity components, respectively. This modeling of the GPS noise is not realistic and colored noise should be considered instead. Nonetheless, the contribution of GPS noise is negligible compared to the noise introduced by the contact transformation.

### A. Scenario 1

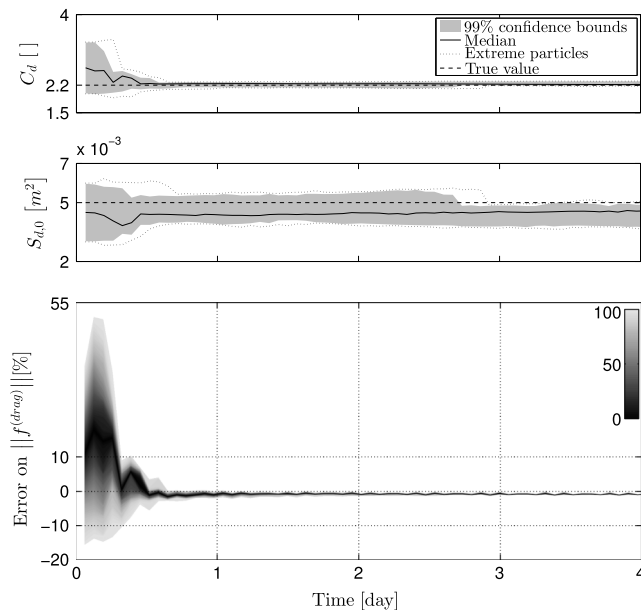
In this scenario, the distributions of the HMM are streamlined by using a single kernel for the GMM and  $m = 0$ , so that both the measurement and process noise are modeled as white noises. Because the filter's propagator and the simulated environment share the same orbital perturbations, process noise is only due to the approximations introduced to achieve the analytical solution in [25].

Figure 2 depicts the convergence of the parameters and the error in the averaged drag. Very broad and biased initial PDFs of the parameters are deliberately exploited to emphasize the robustness of the algorithm. Specifically, we used

$$p_0 \sim \mathcal{U} \left( \begin{bmatrix} 0.8C_d^{(\text{true})} \\ 0.1S_{d,0}^{(\text{true})} \end{bmatrix}, \begin{bmatrix} 1.6C_d^{(\text{true})} \\ 1.7S_{d,0}^{(\text{true})} \end{bmatrix} \right) \quad (29)$$

where  $C_d^{(\text{true})}$  and  $S_{d,0}^{(\text{true})}$  are the values listed in Table 3, and  $\mathcal{U}(a, b)$  denotes the multivariate uniform distribution with lower and upper bounds  $a$  and  $b$ , respectively. Dotted curves denote the envelope of the particles, whereas shaded regions outline 99% confidence bounds deduced by the empirical measure of Eq. (5). After resampling, the envelope is narrowed down to gather particles close to the high-confidence region.

Both  $C_d$  and  $S_{d,0}$  are not converging to the true value, and the mean relative error of  $S_{d,0}$  is particularly pronounced (almost 20%) because its contribution to the ballistic coefficient is less important compared to  $C_d$ . Nonetheless, convergence of the averaged drag is faster, and error drops below 1% after barely 15 iterations, which correspond to about one day. Such enhanced performance is due to the relevant negative correlation between  $C_d$  and  $S_{d,0}$  depicted in Fig. 3. This finding can be generalized: the joint convergence of the parameters is



**Fig. 2** Scenario 1. Convergence of the parameters  $P$  and error in the averaged aerodynamic force. Shades of gray in the bottom figure denote the confidence level.

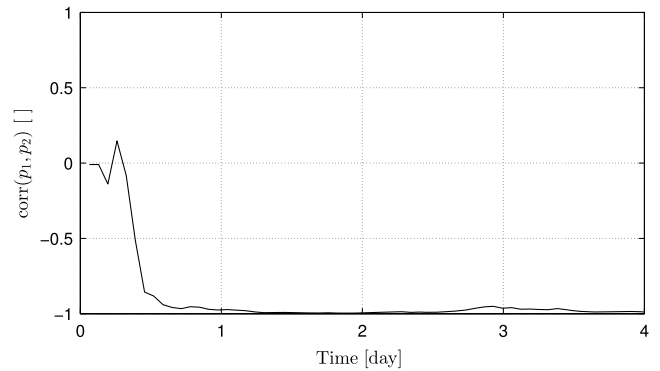


**Fig. 3** Scenario 1. Correlation ( $\text{corr}$ ) between  $C_d$  and  $S_{d,0}$ .

aimed at minimizing error in the nongravitational force and not in the single components of  $p$ .

### B. Scenario 2

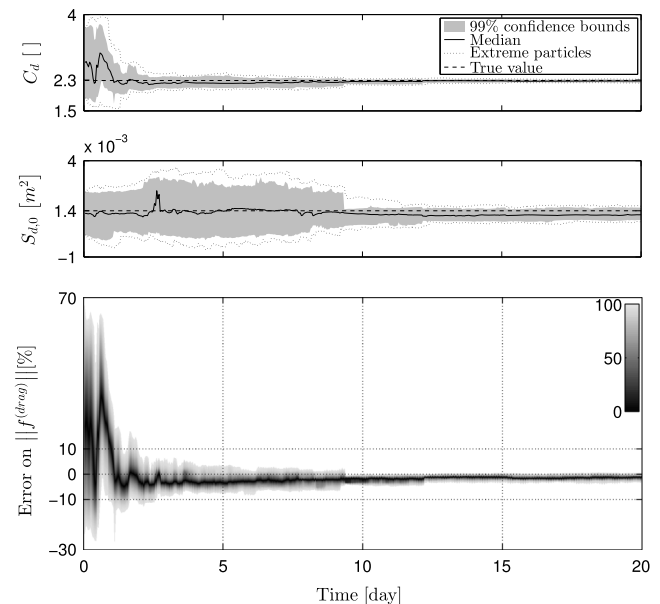
This simulation serves as a transition from the previous example to a more realistic scenario. Process noise is now dominated by neglected perturbations. The filter's time step is now set to 1 h to take advantage of the relevant correlations illustrated in Fig. 1.

The convergence of parameters and error in the averaged aerodynamic force is illustrated in Fig. 4. The same qualitative behavior of the previous case study is observed, although the convergence rate is unsurprisingly reduced because of the more severe process noise. The error stabilizes below 10% after a couple of days, and it does not exceed this threshold because space weather dynamics are neglected, and the orbital decay is moderate within the simulation window.

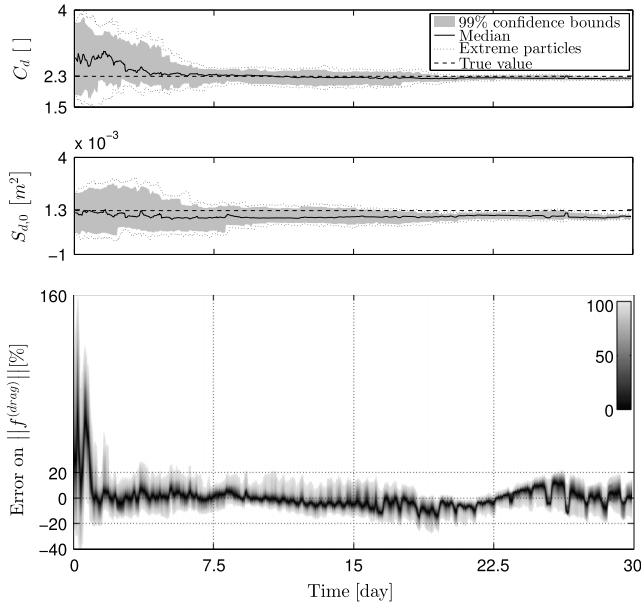
### C. Scenario 3

Figure 5 depicts the convergence of the present case study. Although confidence bounds of  $P$  after about 20 days are comparable to the bounds obtained in the second scenario, the error in the averaged aerodynamic force is larger and unsteady.

Increasing the number of particles in this scenario does not improve the accuracy of the estimation error in the drag because this qualitatively different behavior is due to solar activity, which is a



**Fig. 4** Scenario 2. Convergence of the parameters  $P$  and error in the averaged aerodynamic force. Shades of gray in the bottom figure denote the confidence level.



**Fig. 5 Scenario 3. Convergence of the parameters  $P$  and error in the averaged aerodynamic force. Shades of gray in the bottom figure denote the confidence level.**

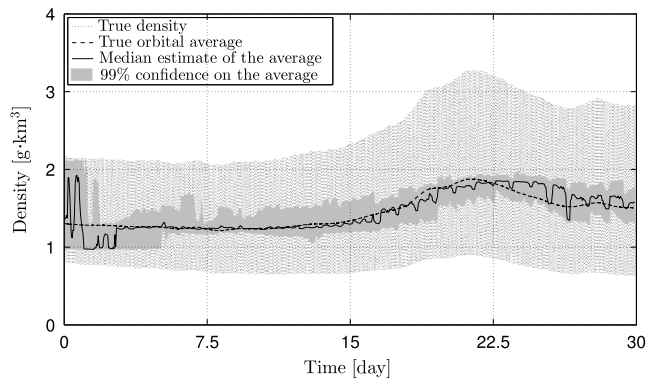


**Fig. 6 Scenario 3. Dotted and dashed curves denote atmospheric density and its orbital average, respectively.**

stochastic process in nature. For this reason, we cannot mitigate its impact on the uncertainty in the aerodynamic force without using other data than satellite state observations. Figure 6 shows the evolution of the averaged drag, which varies up to 50% during the simulation. The trend is captured within the 99% confidence bounds of the estimation, but these bounds remain relatively large in time; they are thus responsible for the broad distribution of the estimation error. We reiterate that the filter ignores the current value of the solar activity. Enhanced performance can be achieved by providing additional information on some space weather proxies to the filter and by correlating them with  $\Lambda$ . Nonetheless, we note that the estimation error is still below 20%. We believe that this is a significant result given the modest data used by the filter and the large amount of uncertainty related to the use of mean elements and a simple analytical propagator.

The current scenario uses the most realistic environment and the least computationally demanding filter among the proposed case studies; so, we wish to briefly comment on the possibility to implement the algorithm on board. Because the filter's time step can be rather large, the computational time to accomplish one iteration is not critical even for low-end microcontrollers. Available memory is the main issue. On top of the memory required to store and evaluate the PDFs of the model and to perform basic algebraic operations, two sets of particles need to be held in memory. Recalling that one particle

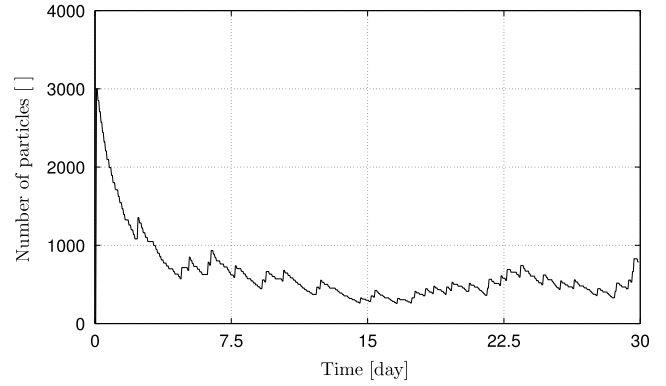


**Fig. 7 Scenario 3. Number of samples as a function of time.**

is defined according to Eq. (4) and assuming double-precision variables, the memory required to store two particle sets is

$$2n[m \dim(\mathbf{X}) + \dim(\mathbf{P}) + 1]8 \text{ B} \quad (30)$$

where 8 B is the size of one double-precision variable. This number can be reduced by noting that  $m - 1$  past states are shared by the two sets, but we consider the conservative value of Eq. (30) in the context of this gross estimation. Figure 7 illustrates the number of samples used during the simulation. Once the estimation is sufficiently converged, the filter uses less than 500 samples on average, which correspond to 192 kB according to Eq. (30). With these caveats in mind, the algorithm should be reasonably implementable on microcontrollers with 512 kB of memory.

#### D. Scenario 4

The filter of this case study uses numerical integration to propagate particles, which enables the possibility to compute both the instantaneous aerodynamic and SRP forces. Uniform uncertainty of  $\pm 20\%$  on all coefficients of the series expansion of Eq. (28) is used at the initial step.

The convergence of the error in the aerodynamic force is illustrated in Fig. 8. After the fourth day, the variance of the error grows up. The same qualitative behavior is also observed, and even accentuated, when the number of particles is increased, as depicted in Fig. 9, where 50,000 particles are used to carry out the estimation. This mechanism is due to the fact that the second-order harmonic expansion used to model the density cannot mimic the whole complexity of the atmosphere. Hence, once the estimation process has sufficiently converged, the diversity of the particles is highly reduced and the Fourier coefficients are stuck in a very narrow support. To mitigate this issue, it is possible to add a rejuvenation step after resampling to reintroduce some diversity as discussed in [26]. However, this result outperforms the previous one because the instantaneous force is now estimated, which exhibits variations of one order of magnitude due to

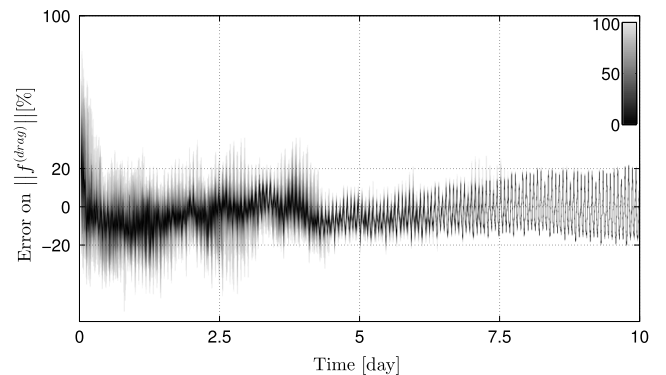


**Fig. 8 Scenario 4. Error in the instantaneous aerodynamic force. Shades of gray denote the confidence level.**

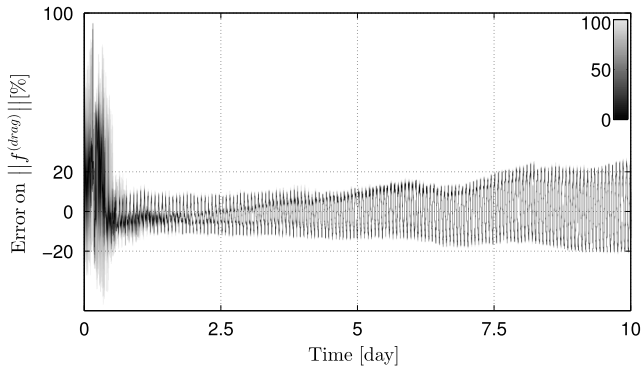


Fig. 9 Scenario 4. Estimation by using 50,000 samples. Error in the instantaneous aerodynamic force. Shades of gray denote the confidence level.

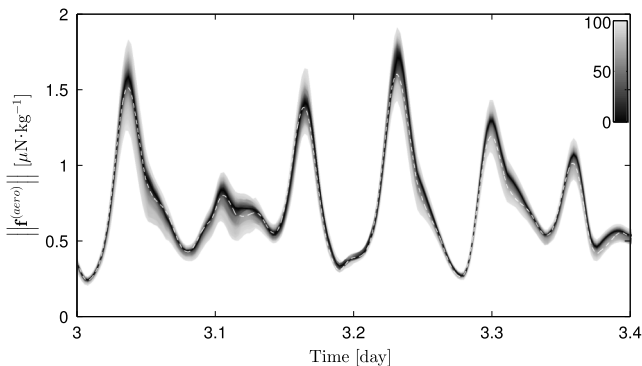


Fig. 10 Scenario 4. Aerodynamic force estimation. The white-dashed line represents the true force.

orbital eccentricity, day–night atmospheric variations, and Earth's oblateness. In particular, we note that even advanced atmospheric models may have local differences on the order of several tens of percent. Figure 10 shows that these variations are adequately captured by the filter.

In this scenario, the number of particles is always larger than 1000 because of the smaller filter's time step and the greater dimension of the problem, which facilitates degeneracy. We also note that the various states and parameters are not equally important. For example, because of the small filter's time step, the marginal PDF of the process noise of the states  $P_1$ ,  $P_2$ ,  $Q_1$ , and  $Q_2$  is much narrower than their corresponding marginal of the measurement noise, so that the contribution of their observations is practically insignificant for the purposes of the estimation. If more parameters have to be estimated (e.g., more harmonics for the atmospheric density or a different perturbation model are used), the curse of dimensionality may occur because of the high dimension of the problem. In this case, more advanced formulations of the filter should be considered (e.g., Hamiltonian Monte Carlo [27] or particle flow [28,29] and optimal transport [30]), for which the key idea is to continuously introduce the effects of the observations to let particles gradually migrate toward peaks of the likelihood.

Finally, the convergence of the reflectivity coefficient is depicted in Fig. 11. The estimation of this parameter is not striking because, as claimed in Sec. IV.A, the filter minimizes the error in the nongravitational force so that it cannot distinguish between its two components: the aerodynamic force, which is estimated with 20% accuracy, is one order of magnitude larger than the SRP so that the latter has a minor impact on the evolution of the averaged elements and, consequently, on the inference of the particles weights. Nonetheless, the reflectivity coefficient is estimated with less than a 20% accuracy, which is not completely despicable considering that the algorithm ignores the physical bounds of  $C_r$ .

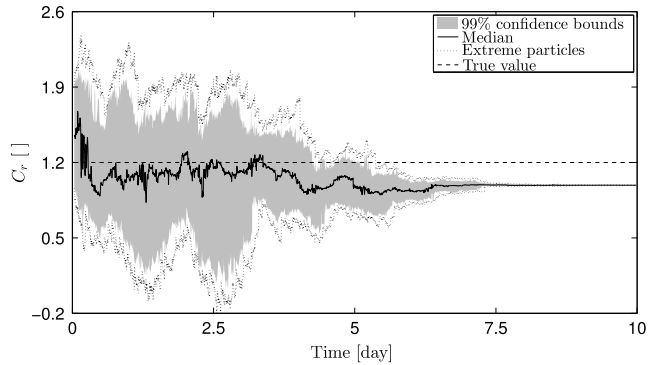


Fig. 11 Scenario 4. True and estimated reflectivity coefficients.

## V. Conclusions

The filter proposed herein does not require in situ accelerometers. Sequential measurements of mean orbital elements are processed instead. The secular effects of nongravitational perturbations allow good particles to be identified after a sufficient training period, even when coarse and arguably sporadic measurements are used.

High-fidelity numerical simulations show that nongravitational forces can be estimated within a 20% error using a first-order contact transformation and no information on the actual solar activity. This result is strongly dependent on the specific underlying orbital propagator, which has to be chosen according to the available computational resources. However, the methodology is presented in a general framework, which can be straightforwardly adapted to any desired propagator ranging from numerical brute-force integration to semianalytical or analytical techniques.

## Appendix A: Gauss Variational Equations for Equinoctial Elements

Let  $a$ ,  $e$ ,  $i$ ,  $\omega$ ,  $\Omega$ , and  $f$  be the classical orbital elements, namely, the semimajor axis, the eccentricity, the orbital inclination, the argument of perigee, the right ascension of the ascending node, and the true anomaly, respectively. Equinoctial elements are defined as [31]

$$\mathcal{E} = \left( a, P_1 = e \sin(\omega + \Omega), P_2 = e \cos(\omega + \Omega), Q_1 = \tan \frac{i}{2} \sin \Omega, \right. \\ \left. Q_2 = \tan \frac{i}{2} \cos \Omega, L = \omega + \Omega + f \right)^T$$

Here,  $L$  is referred to as true longitude.

The GVEs for the equinoctial elements are [31]

$$\dot{a} = \frac{2a^2}{h} \left[ (P_2 \sin L - P_1 \cos L) f_{p,r} + \frac{p}{r} f_{p,t} \right] \\ \dot{P}_1 = \frac{r}{h} \left[ -\frac{p}{r} \cos L f_{p,r} + \left( P_1 + \left( 1 + \frac{p}{r} \right) \sin L \right) f_{p,t} \right. \\ \left. - P_2 (Q_1 \cos L - Q_2 \sin L) f_{p,h} \right] \\ \dot{P}_2 = \frac{r}{h} \left[ \frac{p}{r} \sin L f_{p,r} + \left( P_2 + \left( 1 + \frac{p}{r} \right) \cos L \right) f_{p,t} \right. \\ \left. + P_1 (Q_1 \cos L - Q_2 \sin L) f_{p,h} \right] \\ \dot{Q}_1 = \frac{r}{2h} (1 + Q_1^2 + Q_2^2) \sin L f_{p,h} \\ \dot{Q}_2 = \frac{r}{2h} (1 + Q_1^2 + Q_2^2) \cos L f_{p,h} \\ \dot{L} = \frac{h}{r^2} - \frac{r}{h} (Q_1 \cos L - Q_2 \sin L) f_{p,h}$$

where  $p$ ,  $r$ ,  $h$ ,  $f_{p,r}$ ,  $f_{p,t}$ , and  $f_{p,h}$  are the semilatus rectum, the magnitude of the position vector and angular momentum, and the components of the specific perturbing force in the local-vertical/local-horizontal frame, respectively.

## Appendix B: Analytical Propagator

Near-Circular Orbits in the Uniform Density of an Oblate Planet. Let  $\bar{a}_\tau$ ,  $\bar{e}_\tau$ ,  $\bar{i}_\tau$ ,  $\bar{\omega}_\tau$ ,  $\bar{\Omega}_\tau$ , and  $\bar{M}_\tau$  be the averaged classical orbital elements at the initial time. Here, the averaged mean anomaly  $\bar{M}_\tau$  is considered instead of its true counterpart. Assuming near circular orbits [i.e.,  $\mathcal{O}(\bar{e}_\tau^2) = 0$ ] and uniform atmospheric density  $\rho$ , analytical propagation of the averaged equinoctial elements according to [25] is given by

$$\begin{aligned}\bar{a}_{\tau+1} &= \bar{a}_\tau - C_b \rho \sqrt{\mu \bar{a}_\tau} \Delta t + \frac{1}{4} (C_b \rho \sqrt{\mu \bar{a}_\tau} \Delta t)^2 \\ \bar{P}_{1,\tau+1} &= \frac{\bar{e}_\tau}{\sqrt{\bar{a}_\tau}} \left[ \sqrt{\bar{a}_\tau} - \frac{1}{2} C_b \rho \sqrt{\mu} \Delta t \right] \sin \bar{\omega}_{\tau+1} \\ \bar{P}_{2,\tau+1} &= \frac{\bar{e}_\tau}{\sqrt{\bar{a}_\tau}} \left[ \sqrt{\bar{a}_\tau} - \frac{1}{2} C_b \rho \sqrt{\mu} \Delta t \right] \cos \bar{\omega}_{\tau+1} \\ \bar{Q}_{1,\tau+1} &= \tan \frac{\bar{i}_\tau}{2} \sin \left[ \bar{\Omega}_\tau - \frac{k_2 \cos \bar{i}_\tau}{C_b \rho \mu} \left( \frac{1}{\bar{a}_{\tau+1}^3} - \frac{1}{\bar{a}_\tau^3} \right) \right] \\ \bar{Q}_{2,\tau+1} &= \tan \frac{\bar{i}_\tau}{2} \cos \left[ \bar{\Omega}_\tau - \frac{k_2 \cos \bar{i}_\tau}{C_b \rho \mu} \left( \frac{1}{\bar{a}_{\tau+1}^3} - \frac{1}{\bar{a}_\tau^3} \right) \right] \\ \bar{l}_{\tau+1} &= \bar{l}_\tau + \frac{\sqrt{\mu} (\sqrt{\bar{a}_\tau} + \sqrt{\bar{a}_{\tau+1}})}{2 \bar{a}_\tau \bar{a}_{\tau+1}} \\ &\times \left[ 1 - \frac{k_2 (-4 \cos^2 \bar{i}_\tau + \cos \bar{i}_\tau + 1)}{\mu} \frac{(\bar{a}_\tau^2 + \bar{a}_\tau \bar{a}_{\tau+1} + \bar{a}_{\tau+1}^2)}{\bar{a}_\tau^2 \bar{a}_{\tau+1}^2} \right] \Delta t\end{aligned}$$

where

$$\begin{aligned}\bar{\omega}_{\tau+1} &= \bar{\omega}_\tau + \bar{\Omega}_\tau - \frac{k_2 (-5 \cos^2 \bar{i}_\tau + 2 \cos \bar{i}_\tau + 1)}{4 \sqrt{\mu} \bar{a}_\tau^3 \bar{a}_{\tau+1}^3} \\ &\times (\bar{a}_\tau^2 + \bar{a}_\tau \bar{a}_{\tau+1} + \bar{a}_{\tau+1}^2) \left( \sqrt{\bar{a}_\tau} + \sqrt{\bar{a}_{\tau+1}} \right) \Delta t\end{aligned}$$

and  $\mu$ ,  $\Delta t$ , and  $\bar{l} = \bar{\omega} + \bar{\Omega} + \bar{M}$  denote the Earth's gravitational parameter, the time step, and the averaged mean longitude, respectively. The constant  $k_2$  is defined as  $k_2 = (\mu J_2 r_{\text{eq}}^2 / 2)$ , with  $r_{\text{eq}}$  being the mean equatorial radius.

## Acknowledgments

This work was partially supported by the Belgian National Fund for Scientific Research (FNRS) and by the European Research Council Starting Independent Researcher grant 278231: Flight Algorithms for Disaggregated Space Architectures.

## References

- [1] Gotlib, V. M., Evlanov, E. N., Zubkov, B. V., Linkin, V. M., Manukin, A. B., Podkolzin, S. N., and Rebrov, V. I., "High-Sensitivity Quartz Accelerometer for Measurements of Small Accelerations of Spacecraft," *Cosmic Research*, Vol. 42, No. 1, Jan. 2004, pp. 54–59. doi:10.1023/B: COSM.0000017562.59500.d3
- [2] Tapley, B. D., Schutz, B. E., and Born, G. H., "Fundamentals of Orbit Determination," *Statistical Orbit Determination*, 2004, pp. 159–284. doi:10.1016/B978-0-12683630-1/50023-0
- [3] Tapley, B. D., Neto, A. R., and Schutz, B. E., "Orbit Determination in the Presence of Atmospheric Drag Errors," *Satellite Dynamics*, 1975, pp. 154–169. doi:10.1007/978-3-642-46319-8
- [4] Winn, C. B., "Optimal Estimation of Unmodeled Accelerations on the ONERA Navigational Satellite," *Journal of Spacecraft and Rockets*, Vol. 12, No. 2, Feb. 1975, pp. 79–82. doi:10.2514/3.27812
- [5] Zhang, J., Zhang, K., Grenfell, R., and Deakin, R., "GPS Satellite Velocity and Acceleration Determination Using the Broadcast Ephemeris," *Journal of Navigation*, Vol. 59, No. 2, April 2006, p. 293. doi:10.1017/S0373463306003638
- [6] Wright, J., and Woodburn, J., "Real-Time Estimation of Local Atmospheric Density," *AAS/AIAA Space Flight Mechanics Conference*, American Astronomical Soc. Paper AAS-03-164, Washington, D.C., Feb. 2003.
- [7] Wright, J., and Woodburn, J., "Simultaneous Real-Time Estimation of Atmospheric Density and Ballistic Coefficient," *AAS/AIAA Space Flight Mechanics Conference*, American Astronomical Soc. Paper AAS-04-175, Washington, D.C., Feb. 2004.
- [8] Bowman, B. R., and Moe, K., "Drag Coefficient Variability at 175–500 km from the Orbit Decay Analyses of Spheres," *Advances in the Astronautical Sciences*, Vol. 123, 2005, pp. 117–136.
- [9] Saunders, A., Swinerd, G. G., and Lewis, H. G., "Deriving Accurate Satellite Ballistic Coefficients from Two-Line Element Data," *Journal of Spacecraft and Rockets*, Vol. 49, No. 1, Jan. 2012, pp. 175–184. doi:10.2514/1.A32023
- [10] Lubey, D. P., and Scheeres, D. J., "Identifying and Estimating Mismodeled Dynamics via Optimal Control Policies and Distance Metrics," *Journal of Guidance, Control, and Dynamics*, Vol. 37, No. 5, Sept. 2014, pp. 1512–1523. doi:10.2514/1.G000369
- [11] Doucet, A., Godsill, S., and Andrieu, C., "On Sequential Monte Carlo Sampling Methods for Bayesian Filtering," *Statistics and Computing*, Vol. 10, No. 3, 2000, pp. 197–208. doi:10.1023/A:1008935410038
- [12] Doucet, A., Freitas, N., and Gordon, N., (eds.), *Sequential Monte Carlo Methods in Practice*, Springer Science + Business Media, New York, 2001, pp. 3–14, 79–95. doi:10.1007/978-1-4757-3437-9
- [13] McCabe, J. S., and DeMars, K. J., "Particle Filter Methods for Space Object Tracking," *AIAA/AAS Astrodynamics Specialist Conference*, AIAA Paper 2014-4308, Aug. 2014. doi:10.2514/6.2014-4308
- [14] Kim, Y. R., Park, S.-Y., Park, C., Park, E.-S., and Lim, H.-C., "Precise Orbit Determination with Satellite Laser Ranging Observations Using a Batch Filter Based on Particle Filtering," *AIAA/AAS Astrodynamics Specialist Conference*, AIAA Paper 2012-5064, Aug. 2012. doi:10.2514/6.2012-5064
- [15] Mashiku, A., Garrison, J., and Carpenter, J. R., "Statistical Orbit Determination Using the Particle Filter for Incorporating Non-Gaussian Uncertainties," *AIAA/AAS Astrodynamics Specialist Conference*, AIAA Paper 2012-5063, Aug. 2012. doi:10.2514/6.2012-5063
- [16] Zeng, G., Hu, M., and Yao, H., "Relative Orbit Estimation and Formation Keeping Control of Satellite Formations in Low Earth Orbits," *Acta Astronautica*, Vol. 76, July 2012, pp. 164–175. doi:10.1016/j.actaastro.2012.02.024
- [17] Hwang, S. S., and Speyer, J. L., "Particle Filters with Adaptive Resampling Technique Applied to Relative Positioning Using GPS Carrier-Phase Measurements," *IEEE Transactions on Control Systems Technology*, Vol. 19, No. 6, Nov. 2011, pp. 1384–1396. doi:10.1109/TCST.2010.2091415
- [18] Daum, F., "Nonlinear Filters: Beyond the Kalman Filter," *IEEE Aerospace and Electronic Systems Magazine*, Vol. 20, No. 8, Aug. 2005, pp. 57–69. doi:10.1109/MAES.2005.1499276
- [19] Liu, J., and West, M., "Combined Parameter and State Estimation in Simulation-Based Filtering," *Sequential Monte Carlo Methods in Practice*, Springer Science + Business Media, New York, 2001, pp. 197–223. doi:10.1007/978-1-4757-3437-9\_10
- [20] Brouwer, D., "Solution of the Problem of Artificial Satellite Theory Without Drag," *Astronomical Journal*, Vol. 64, Nov. 1959, p. 378. doi:10.1086/107958
- [21] Lyddane, R. H., "Small Eccentricities or Inclinations in the Brouwer Theory of the Artificial Satellite," *Astronomical Journal*, Vol. 68, Oct. 1963, pp. 555–558. doi:10.1086/109179
- [22] Dell'Elce, L., Arnst, M., and Kerschen, G., "Probabilistic Assessment of the Lifetime of Low-Earth-Orbit Spacecraft: Uncertainty Characterization," *Journal of Guidance, Control, and Dynamics*, Vol. 38, No. 5, May 2015, pp. 900–912. doi:10.2514/1.G000148
- [23] Doombos, E., *Thermospheric Density and Wind Determination from Satellite Dynamics*, Springer, Berlin, 2012, pp. 63–74. doi:10.1007/978-3-642-25129-0

- [24] Picone, J. M., Hedin, A. E., Drob, D. P., and Aikin, A. C., "NRLMSISE-00 Empirical Model of the Atmosphere: Statistical Comparisons and Scientific Issues," *Journal of Geophysical Research: Space Physics*, Vol. 107, 2002.
- [25] Martinusi, V., Dell'Elce, L., and Kerschen, G., "Analytic Propagation of Near-circular Satellite Orbits in the Atmosphere of an Oblate Planet," *Celestial Mechanics and Dynamical Astronomy*, Vol. 123, No. 1, June 2015, pp. 85–103.  
doi:10.1007/s10569-015-9630-7
- [26] Gilks, W. R., and Berzuini, C., "Following a Moving Target-Monte Carlo Inference for Dynamic Bayesian Models," *Journal of the Royal Statistical Society: Series B, Statistical Methodology*, Vol. 63, No. 1, Feb. 2001, pp. 127–146.  
doi:10.1111/rssb.2001.63.issue-1
- [27] Girolami, M., and Calderhead, B., "Riemann Manifold Langevin and Hamiltonian Monte Carlo Methods," *Journal of the Royal Statistical Society: Series B, Statistical Methodology*, Vol. 73, No. 2, March 2011, pp. 123–214.  
doi:10.1111/rssb.2011.73.issue-2
- [28] Daum, F., and Huang, J., "Nonlinear Filters with Particle Flow Induced by Log-Homotopy," *Signal Processing, Sensor Fusion, and Target Recognition XVIII*, edited by Kadar, I., SPIE-International Society for Optical Engineering, Bellingham, WA, May 2009.  
doi:10.1117/12.814241
- [29] de Melo, F. E., Maskell, S., Fasiolo, M., and Daum, F., "Stochastic Particle Flow for Nonlinear High-Dimensional Filtering Problems," 2015, <https://arxiv.org/pdf/1511.01448>.
- [30] Reich, S., "A Dynamical Systems Framework for Intermittent Data Assimilation," *BIT Numerical Mathematics*, Vol. 51, No. 1, Dec. 2010, pp. 235–249.  
doi:10.1007/s10543-010-0302-4
- [31] Battin, R. H., *An Introduction to the Mathematics and Methods of Astrodynamics*, Revised ed., AIAA, Reston, VA, Jan. 1999, pp. 490–494.  
doi:10.2514/4.861543